

Optomechanical THz detection with a sub-wavelength resonator

Cherif Belacel, Yanko Todorov, Stefano Barbieri, Djamel Gacemi, Ivan Favero, and Carlo Sirtori

Laboratoire Matériaux et Phénomènes Quantiques, Université Paris Diderot, Sorbonne Paris Cité, CNRS-UMR 7162, 75013 Paris, France

Abstract. The terahertz spectral domain offers a myriad of applications spanning chemical spectroscopy, medicine, security and imaging [1], it has also recently become a playground for fundamental studies of light-matter interactions [2-6]. Terahertz science and technology could benefit from optomechanical approaches, which harness the interaction of light with miniature mechanical resonators [7,8]. So far, optomechanics has mostly focused on the optical and microwave domains, leading to new types of quantum experiments [9-11] and to the development of optical-microwave converters [12-14]. Here we propose and validate the concept of terahertz optomechanics, by coupling far-infrared photons to the mechanical degrees of freedom of the flexible part of a sub-wavelength split-ring resonator [15]. The resulting mechanical signal is read-out optically, allowing our semiconductor/metal device to operate as a compact and efficient terahertz detector with a noise equivalent power of 8 nW/√Hz and a linear dynamics over five decades. Furthermore, our device operates at room temperature and at high-frequency (>10MHz), well beyond the response speed of Golay cells, pyroelectric detectors and cryogenic semiconductor bolometers [16,17]. These properties makes it already ideally suited for applications relying on high speed bright terahertz sources such as quantum cascade lasers [18,19] and synchrotrons [20]. Moreover the optomechanical element introduced in this work is suitable for integration on local probes or within imaging arrays, opening new prospects for sensing in the terahertz domain.

The device realized in this work is shown in Figure 1 and consists of an asymmetric split ring resonator (SRR), obtained by depositing a metal pattern on a GaAs/AlGaAs layered semiconductor structure. By using standard semiconductor etching technology, the narrow arm of the resonator has been processed into a cantilever (Fig. 1a) with a high aspect ratio (width $w=581\text{nm}$, thickness $t=470\text{nm}$ and length $L=17.2\mu\text{m}$). As shown in Fig. 1b the free end of the cantilever completes the 309 nm wide capacitive gap (d_{gap}) of the SRR. The geometrical dimensions of the SRR, as indicated in Fig. 1b have been chosen to set its fundamental electromagnetic resonance in the THz domain. When this resonance is excited by the incident Tera Hertz (THz) radiation, a dynamic distribution of charges with opposite signs appears on both sides of the gap (Fig. 1b). This results into a quasi-static Coulomb force that attracts the cantilever towards the opposite end of the gap and sets it in motion. The amplitude of this mechanical movement is directly related to the intensity of the incident THz wave, and, as explained further below, is read out optically with sub-picometer precision.

In Figure 2, we present the dual characteristics of our structure, which behaves both as an electromagnetic (Fig.2a) and mechanical (Fig.2b) resonator. The SRR THz response has been measured in transmission spectroscopy with a Fourier Transform Interferometer and a cooled Ge bolometer (see Methods). In order to increase the amplitude of the transmission features we used a dense array of nominally identical SRRs [21,22]. The SRR resonance appears in the spectrum of Fig. 2a as a Lorentzian dip with a central frequency $\omega_{\text{THz}}/2\pi=2.7\text{ THz}$ and a quality factor $Q_{\text{THz}}=8.4$. These characteristics are in good agreement with numerical modelling based on a finite elements method. The inset of Fig. 2a shows the resonant electric field E_z normal to the top metal surface of the SRR obtained from these simulations. While the field is strongest around the gap, it spreads along the structure indicating the presence of propagation effects. Indeed, the SRR resonant wavelength is well recovered from the formula $\lambda_{\text{res}}=2n_{\text{eff}}P$, where $P=44.5\mu\text{m}$ is the medium perimeter of the SRR loop, and $n_{\text{eff}}=1.2$ is an effective index that takes into account the field leakage around the structure (see Methods). According to Gauss's theorem the field E_z provides the surface charge density on the metal plates induced at resonance by the impinging THz radiation [23]. The resulting Coulomb force is strongest around the SRR gap, where the distance between the charges is smallest, and excites the cantilever movement in the plane of the SSR.

The cantilever itself is a mechanical resonator, with both in-plane and out of plane flexural modes [24]. Its movement was read-out with a balanced optical detection scheme using a near infrared (NIR) diode laser ($\lambda=940\text{nm}$) (see Methods). This scheme is sufficiently sensitive to resolve the cantilever Brownian motion, as shown in Fig. 2b, on the fundamental in-plane flexural mode. A numerical simulation of this mode is shown in the inset of Fig.2b. The Brownian motion is well fitted by the analytical expression of the noise spectral power density $S_{xx}(f)$ from a damped mechanical oscillator model [8] (Methods). From this fit we extract a mechanical

frequency $\omega_m/2\pi=957\text{kHz}$ and a quality factor $Q_m=93$. The knowledge of the cantilever dimension and composition allows determining precisely the effective mass $m_{\text{eff}}=10.7\text{pg}$, which is in agreement with the measured frequency (see Methods). From this value we infer the room temperature peak noise spectral density $S_{xx}(f_m)=2k_B T Q_m/m_{\text{eff}}\omega_m^3=0.33\text{pm}^2/\text{Hz}$, which allowed the calibration of the cantilever displacements measured by the balanced detection scheme.

The cantilever movement under the influence of THz radiation can be described by the following equation of motion, derived from an effective capacitor-inductance model of the SRR (Methods):

$$(1) \quad \frac{d^2 x}{dt^2} + \frac{\omega_m}{Q_m} \frac{dx}{dt} + \omega_m^2 x = - \frac{W_{\text{THz}}(t)}{m_{\text{eff}}} \left. \frac{d \ln C_{\text{eff}}}{dx} \right|_{x=d_{\text{gap}}}$$

Here x is the position of the cantilever tip (Fig. 2b), $C_{\text{eff}}(x)$ is the effective capacitance of the charge distribution of the THz mode, and $W_{\text{THz}}(t)$ is the time dependent electric energy stored in the resonator at the THz resonance. Note that the electric energy oscillates in the THz range, $W_{\text{THz}}(t) \sim \cos^2(\omega_{\text{THz}}t)$, i.e. at a frequency that is six orders of magnitude higher than the mechanical frequency ω_m , a situation reminiscent cavity optomechanics at optical frequencies [7]. As a result the cantilever is only sensitive to the value of the electric energy $\langle W_{\text{THz}} \rangle$ averaged over the THz oscillation cycles. The latter can be expressed as $\langle W_{\text{THz}} \rangle = I_{\text{THz}} A_{\text{coll}} Q_{\text{THz}} / 2\omega_{\text{THz}}$, where I_{THz} is the intensity (W/m^2) of the incident THz radiation. The quantity A_{coll} is a collection area, such that $I_{\text{THz}} A_{\text{coll}}$ corresponds to the power dropped in the SSR. Then, according to Eq.(1), the net mechanical effect of a continuous THz wave impinging on the detector is to displace the rest position of the cantilever. This effect can be resonantly exalted if the incident THz intensity is modulated at the mechanical frequency ω_m of the cantilever. For a sinusoidal modulation $I_{\text{THz}}(t) = I_{\text{THz}}^0 (1 + \cos(\omega_m t))$ we can define an internal responsivity of the system as the ratio between the amplitude of the resulting forced mechanical motion x_{max} and the peak THz power $A_{\text{coll}} I_{\text{THz}}^0$ coupled into the SRR:

$$(2) \quad R_{\text{in}} = \frac{x_{\text{max}}}{A_{\text{coll}} I_{\text{THz}}^0} = \frac{Q_m}{2m_{\text{eff}}\omega_m^2} \frac{Q_{\text{THz}}}{d_{\text{gap}}^{\text{eff}} \omega_{\text{THz}}}$$

Eq.(2) clearly reveals the double effect of recycling of the vibration quanta and THz photons in the detection process through the factor $Q_m \times Q_{\text{THz}}$. Here we introduced the effective capacitive gap $d_{\text{gap}}^{\text{eff}} = ((d \ln C_{\text{eff}} / dx)|_{x=d_{\text{gap}}})^{-1}$ which depends on the details of the charge distribution at resonance. For our structure, we estimate $d_{\text{gap}}^{\text{eff}} \sim 546\text{nm}$ based on the improved Palmer formula of the capacitance, which takes into account the effect of fringing fields [25] (Methods). To connect our device with other optomechanical systems [8], we have also evaluated the

frequency pull parameter $g_{om} = \omega_{\text{THz}} / d_{\text{gap}}^{\text{eff}} = 31.4$ GHz/nm and the amplitude of zero-point mechanical motion $x_{\text{ZPF}} = \sqrt{\hbar / 2m_{\text{eff}}\omega_m} = 2.8$ fm, which yield a single-photon optomechanical coupling $g_0 = g_{om}x_{\text{ZPF}}/2 = 0.44$ MHz. This value is commensurable with the mechanical frequency of the cantilever, which, in the quantum regime, would imply the possibility to resolve individual THz photons by recording the quantized mechanical displacement. Such non-demolition ponderomotive probe of electromagnetic energy was already considered in the early work of Braginsky [26], and while it has remained out of reach for optical and microwave optomechanical settings, it could seemingly be accessible in the THz domain.

Using Eq.(2) together with the value of the expression of the peak noise density of the Brownian motion, we obtain an analytical expression of the internal Noise Equivalent Power (NEP) for our structure, defined as $NEP = S_{xx}(f_m)^{1/2} / R_{in}$:

$$(3) \quad NEP = \sqrt{2k_B T m_{\text{eff}} \Gamma_m} \frac{2\omega_{\text{THz}} d_{\text{gap}}^{\text{eff}}}{Q_{\text{THz}}}$$

Here $\Gamma_m = \omega_m / Q_m$ is the linewidth of the mechanical mode. Eqs. (2) and (3), derived for our particular system, can be applied to any other geometry and can be used to optimize the design of optomechanical THz detectors. For the current geometry we obtain $R_{in} \sim 113$ fm/nW and $NEP \sim 4.8$ nW/Hz^{1/2}.

The experimental setting of our THz detection is reported in Fig. 3a. As a THz source, we use a quantum cascade laser (QCL) based on an active region similar to Refs. **27** and **28**, with an emission frequency of 2.5 THz and a maximum output power calibrated at 4.7mW. The THz radiation from the QCL is collected with two parabolic mirrors and focused on a single SRR with the help of a silicon hyperhemispherical lens [29], positioned on the backside of the GaAs substrate. To produce a resonant mechanical effect of the THz QCL was either driven in pulsed mode, or in continuous wave with its current modulated with a signal generator at the frequency $f_{\text{mod}} = \omega_m / 2\pi$. The cantilever oscillation was read-out optically as described in the Methods section. All measurements were performed on a single SRR resonator.

In Figure 3b we provide different spectra of the mechanical response of the cantilever, recorded with an electronic spectrum analyzer (ESA) as a function of the incident THz power. For these spectra, the laser was driven at maximum power (4.7mW) in pulsed mode with a duty cycle of 16.5%, and a frequency $f_{\text{mod}} = 955$ kHz. The incident power on the structure was attenuated with a series of identical absorbers, each providing 30% transmission. The forced cantilever oscillation induced by the THz source clearly appears as a single Dirac-like peak on the top of the Brownian noise. From this data, and using the calibration of the noise spectral density $S_{xx}(f)$ we can determine respectively the amplitude of the cantilever motion and the NEP of the

structure, as shown in Figure 3c and 3d. The amplitude follows the expected linear dependence, remarkably over five orders of magnitude of the incident power. The responsivity and NEP obtained are respectively $R=50\text{fm/nW}$, and $\text{NEP}=8\text{nW/Hz}^{1/2}$. These values differ by less than a factor of two from the theoretical limits derived from Eq.(2) and Eq.(3), meaning that a considerable fraction of the THz radiation is coupled to our resonator. We note however that the quality factor Q_{THz} measured from the array of THz SRRs and used in the evaluation using Eq.(2) is necessarily lower (typically by a factor 4) than the value of a single resonator due to packing effects [21]. With such correction, the fraction of THz radiation coupled in the SRR would be in the order of 10-20%.

To explore further the performance of our optomechanical detector, we studied its behavior as a function of the QCL current modulation frequency f_{mod} . For these measurements, in order to access both amplitude and phase of the driven cantilever motion, the ESA was replaced by a lock-in amplifier (Fig. 3a). In Fig. 4a we show the amplitude of the lock-in signal when f_{mod} is spanned from 70kHz to 18MHz, and a 4.7mW of QCL output power. This graph maps the mechanical transfer function of the driven cantilever movement excited by the THz radiation. Three modes are clearly visible; the $f_1=955\text{kHz}$ mode presented above and two higher order modes, respectively at $f_2=6\text{MHz}$ and $f_3=16.6\text{MHz}$. These values are in excellent agreement with estimates from the formula for clamped bars [24] $f_n=2.81f_1(n-0.5)^2$. In Fig.4b we provide the Brownian noise spectrum of the cantilever in the same frequency range, obtained with the ESA and with the QCL off. In Fig.4c, we plot the detector NEP as derived from the signal Fig.(4a) and noise Fig.(4b) spectra. This graph shows, on one hand, that one can exploit high order mechanical resonances to operate the detector at higher modulation frequencies. On the other hand, for the first two modes, the detector can be operated in frequency bands around the mechanical resonances that are several times wider than their linewidths without heavily compromising on the NEP. This is further illustrated in Figs. 4d,4e and 4f, where we show both the lock-in signal and phase in high resolution scans of f_{mod} around the mechanical resonances. For the first and second order modes the phase remains very well determined for at least $5\Gamma_m$. The typical values (~ 10 MHz) of the modulation frequencies for our system are thus considerably higher than those (10 Hz-100 Hz) allowed by commercially available Golay cells, pyroelectric detectors or semiconductor bolometers [17].

We have thus introduced a new metamaterial based opto-mechanical THz detector that operates at room temperature and allows modulation frequencies that are much higher than those of conventional THz detectors. This scheme is already suitable for applications that rely on powerful THz sources such as QCLs [19]. Reducing the cantilever dimensions or using other types of mechanical resonators can increase even further the modulation frequencies [30]. As indicated by Eq.(3), further improvement of the NEP is achievable by increasing the quality factors of both THz and mechanical resonators. Higher Electromagnetic quality factors Q_{THz} up

to 100-200 are achievable in symmetric resonators [31]. When tested in vacuum, the cantilevers displayed mechanical quality factors on the order of $Q_m=1000-3000$. The planar geometry of our structure is also very convenient for large scale integration for imaging arrays [32], or for packaging the device on a single chip [33]. Furthermore, our structure is based on semiconductor technology and operates in frequency ranges where THz electronic transitions in quantum heterostructures can be achieved [3,34]. Therefore, beyond the detector application, our device concept could open new perspectives for fundamental studies of opto-mechanical and light-matter interaction.

Acknowledgment

We acknowledge financial support from the ANR (Agence Nationale de la Recherche) and CGI (Commissariat à l'Investissement d'Avenir) through Labex SEAM "Capture" project (ANR 11 LABX 086, ANR 11 IDEX 05 02)

Methods See *method section at page 13*

References

- [1] Tonouchi, M. Cutting-edge terahertz technology, *Nature Phot.* **1**, 97 - 105 (2007)
- [2] Gunter, G. et al. Sub-cycle switch-on of ultrastrong light-matter interaction. *Nature* **458**, 178–181 (2009).
- [3] Todorov, Y. et al. Ultrastrong light-matter coupling regime with polariton dots. *Phys. Rev. Lett.* **105**, 196402 (2010)
- [4] Scalari, G. et al. Ultrastrong coupling of the cyclotron transition of a 2D electron gas to a THz metamaterial. *Science* **335**, 1323–1326 (2012)
- [5] Dietze, D., Benz, A., Strasser, G., Unterrainer, K. and Darmo, J. Terahertz meta-atoms coupled to a quantum well intersubband transition. *Opt. Express* **19**, 13700–13706 (2011)
- [6] Pal, S. et al., Ultrawide electrical tuning of light matter interaction in a high electron mobility transistor structure, *Sci. Rep.* **5**, 16812 (2015)
- [7] Favero, I., and Karrai, K. Optomechanics of deformable optical cavities. *Nature Photon.* **3**, 201-209. (2009)
- [8] Aspelmeyer, M., Kippenberg, T. J., and Marquardt, F. Cavity optomechanics. *Rev. Mod. Phys.* **86**, 1391–1452 (2014)
- [9] O'Connell, A. D. et al. Quantum ground state and single-phonon control of a mechanical resonator. *Nature* **464**, 697–703 (2010)
- [10] Teufel, J. D. et al. Sideband cooling of micromechanical motion to the quantum ground state. *Nature* **475**, 359–363 (2011)
- [11] Chan, J. et al. Laser cooling of a nanomechanical oscillator into its quantum ground state. *Nature* **478**, 89–92 (2011)
- [12] Bochmann, J., Vainsencher, A., D. D. Awschalom, and Cleland, A. N., Nanomechanical coupling between microwave and optical photons. *Nature Phys.* **9**, 712–716 (2013)

- [13] Andrews, R. W., *et al.* Bidirectional and efficient conversion between microwave and optical light, *Nature Phys.* **10**, 321–326 (2014)
- [14] Bagci, T., *et al.* Optical detection of radio waves through a nanomechanical transducer, *Nature* **507**, 81–85 (2014)
- [15] Shalaev, V.M. Optical negative-index metamaterials. *Nature Photon.* **1**, 41 - 48 (2007)
- [16] Mittleman, D. *Sensing with Terahertz Radiation* (Springer, 2003).
- [17] Rogalski, A. and Sizov, F. Terahertz detectors and focal plane arrays *Opto-Electron. Rev.* **19**, 346-404 (2011).
- [18] Sirtori, C., Barbieri, S., and Colombelli, R. Wave engineering with THz quantum cascade lasers. *Nature Photon.* **7**, 691-701 (2013).
- [19] Locatelli, M. *et al.* Real-time terahertz digital holography with a quantum cascade laser. *Sci. Rep.* **5**, 13566 (2015)
- [20] Patoka, P. *et al.* Nanoscale plasmonic phenomena in CVD-grown MoS₂ monolayer revealed by ultra-broadband synchrotron radiation based nano-FTIR spectroscopy and near-field microscopy. *Opt. Express* **24**, 1154-1164 (2016)
- [21] Singh, R., Rockstuhl C. and Zhang, W. Strong influence of packing density in terahertz metamaterials. *Appl. Phys. Lett.* **97**, 241108 (2010)
- [22] Feuillet-Palma, C., Todorov, Y., Vasanelli, A. and Sirtori, C. Strong near field enhancement in THz nano-antenna arrays. *Sci. Rep.* **3**, 1361 (2012)
- [23] Jackson, J. D. *Classical Electrodynamics*, (John Wiley & sons, 1999).
- [24] Timoshenko, S. *Vibration problems in engineering*, (D. Van Nostrand Company INC., New York, 1937).
- [25] Leus, V. and Elata, D. *Fringing Field effect in electrostatic actuators* (Technical report, Faculty of mechanical engineering Technion - Israel Institute of Technology, Haifa, Israel, 2004).
- [26] Braginsky, V.B., and Khalili, F. Y. *Quantum Measurement*, (Cambridge University Press, 1992)
- [27] Li, H. *et al.* Coupled-cavity terahertz quantum cascade lasers for single mode operation. *Appl. Phys. Lett.* **104**, 241102 (2014)
- [28] Barbieri, S. *et al.* 2.9 THz quantum cascade laser operating up to 70K in continuous wave, *Appl. Phys. Lett.* **85**, 1674 (2004)
- [29] P. Uhd Jepsen, P.U., and Keiding, S. R. Radiation patterns from lens-coupled terahertz antennas. *Opt. Lett.* **20**, 807-809 (1995)
- [30] Lu Ding, L. *et al.* High Frequency GaAs Nano-Optomechanical Disk Resonator. *Phys. Rev. Lett.* **105**, 263903 (2010)
- [31] I Al-Naib, I., Yang, Y., Dignam, M. M., Zhang W., and Singh, R. Ultra-high Q even eigenmode resonance in terahertz metamaterials. *Appl. Phys. Lett.* **106**, 011102 (2015)
- [32] Tao, H. *et al.* Microwave and Terahertz wave sensing with Metamaterials. *Opt. Express* **19**, 21620-21626 (2011)
- [33] Nguyen, D.T., *et al.* Improved optomechanical disk resonator sitting on a pedestal mechanical shield, *New Journal of Physics*, **17**, 023016 (2015)
- [34] Shibata, K., Umeno, A., Cha, K. M., and Hirakawa, K. Photon-Assisted Tunneling through Self-Assembled InAs Quantum Dots in the Terahertz Frequency Range. *Phys. Rev. Lett.* **109**, 077401 (2012)

Figures & Figure captions

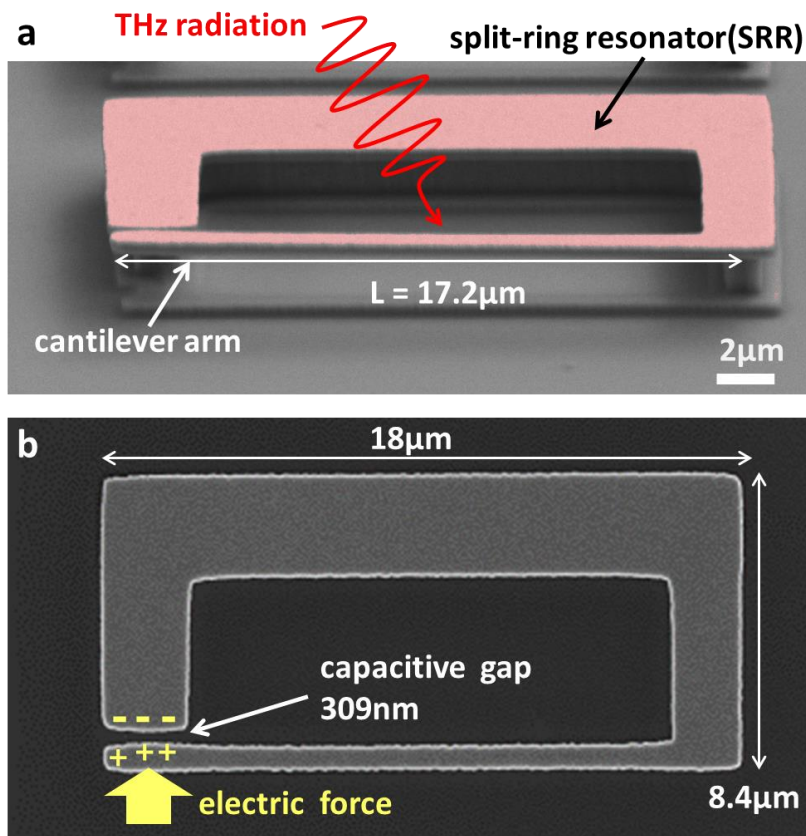


Figure 1: THz optomechanical device a,b Scanning electron microscope picture of the side (1a) and top (1b) of our THz optomechanical detector. As shown in **1a**, the SRR is closed by a $17.2\mu\text{m}$ long cantilever arm. The THz radiation incident on the structure (schematically shown by a red wavy arrow in 1a) excites the SRR resonance, which induces current-charge oscillations in the structure. As indicated in 1b the charges build up around the capacitive gap and give rise to a quasi-static Coulomb that attracts the cantilever towards the opposite side the gap.

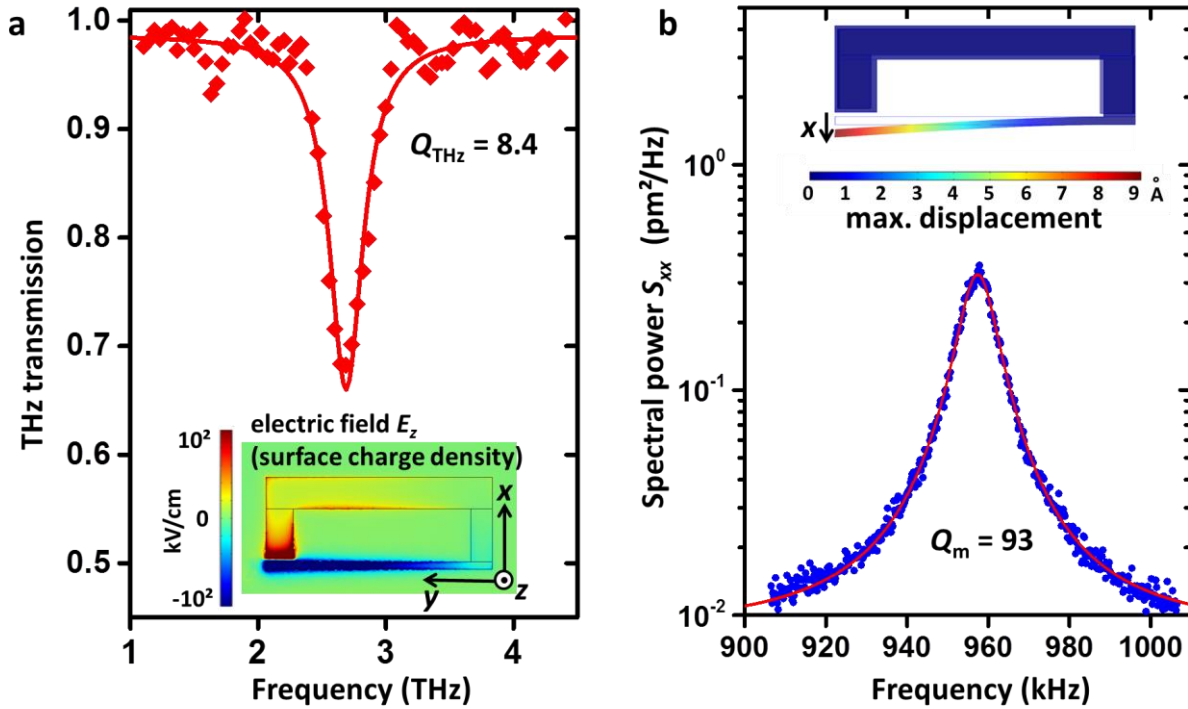


Figure 2: THz and mechanical and characteristics **a**, Far infrared transmission spectrum of an array of identical SRRs obtained with an FTIR spectroscopy an Ge bolometer. The THz beam was focused on the sample with the help of 4 parabolic mirrors. Owe to the large spot-size of the focal point ($\sim 1\text{mm}^2$) we used a dense array of SRRs (see Methods). The inset shows the vertical electric field E_z of the fundamental SRR mode obtained by finite elements method with a commercial software. Since the surface charge density on the metal parts is provided by $\sigma = \epsilon_0 E_z$ [23], this plot also provides the charge distribution excited by the SRR resonance, leading to the quasi-static Coulomb force indicated in Fig. 1b. **b**, Typical spectrum of the Brownian motion of the cantilever, that displays the fundamental in-plane flexural resonance that couples with the THz photons. The spectrum was recorded with an electronic spectrum analyzer with 100Hz resolution bandwidth (Methods). The inset shows a finite elements method simulation of the mechanical mode.

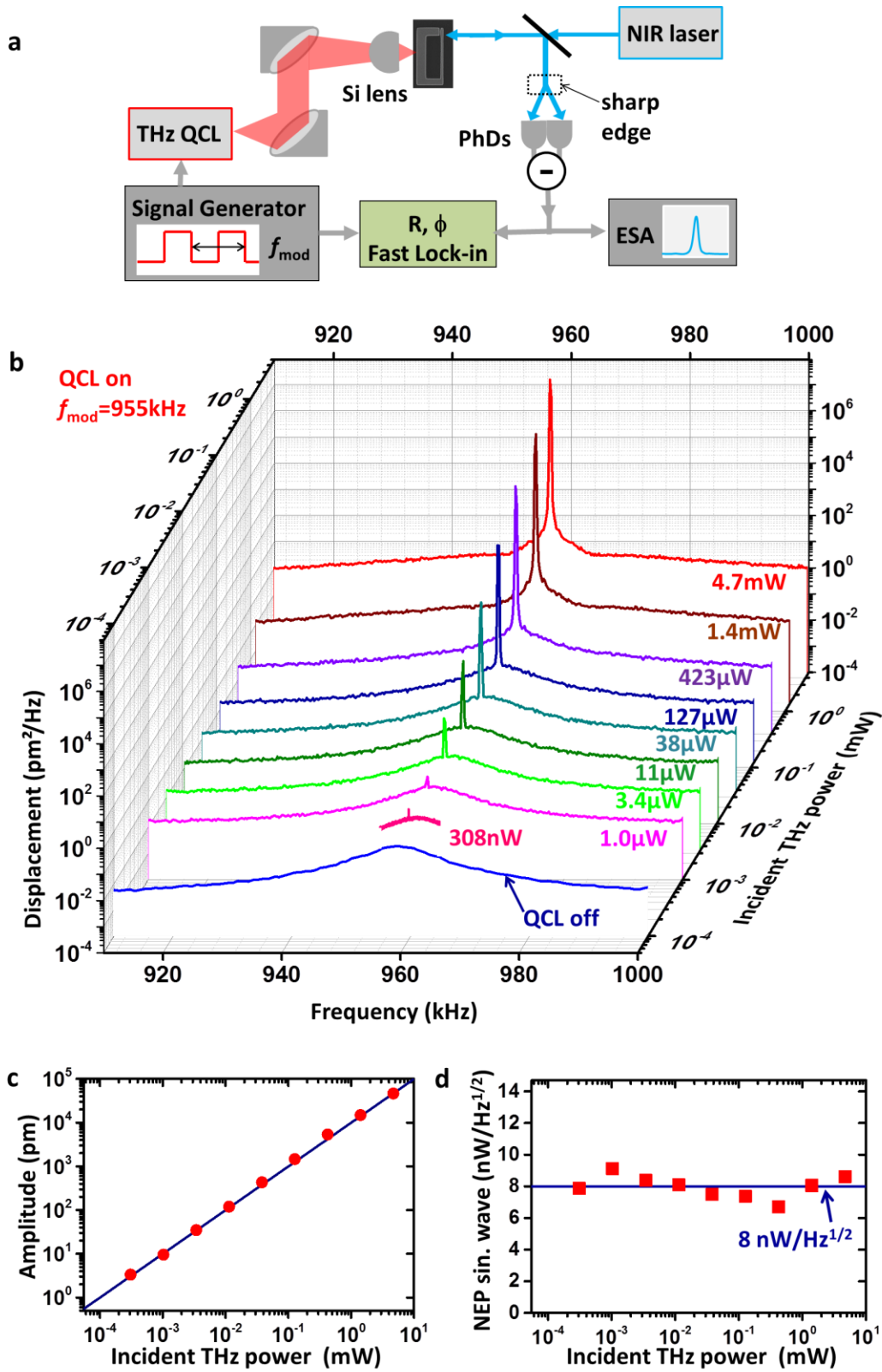


Figure 3: THz optomechanical detection

Figure 3: THz optomechanical detection **a**, Experimental set-up for our THz optomechanical detection scheme. The optical output of the THz QCL is collected with two parabolic mirrors and focused on a single SRR with the help of a silicon hyperhemispherical lens. The QCL drive current is modulated at a frequency f_{mod} , close to the mechanical resonance of the cantilever. The cantilever movement is read-out optically as described in Methods. **b**, Series of spectra recorded by the electronic spectrum analyzer (ESA) at 100Hz resolution bandwidth (RSB) for different attenuation of the THz QCL. For these measurements, the QCL was driven in pulsed mode with a square wave with 16.5% duty cycle and a frequency $f_{mod}=955$ kHz. The first curve of the series “QCL off” is recorded with the QCL not running. The phase noise appearing in the spectra at higher THz powers (42 μ W, 1.4mW and 4.7mW in Fig.3b) reflects the phase noise of the signal generator used to modulate the QCL. **c**, Amplitude of the cantilever movement, obtained from the integral of the modulation peaks in (a) as a function of the incident THz power (dots). The blue line is a linear fit. (d) Direct measurements for the net equivalent power (NEP) of our detector. The fluctuating data points (squares) were obtained from each spectrum in 3b according to the expression $P_{THz} \sqrt{V_{noise}^2 / (RSB \cdot V_{peak}^2)}$ with P_{THz} the value of the incident THz power, V_{peak} the voltage of the modulation peak at f_{mod} , V_{noise} the voltage of the noise spectrum at the same frequency and the QCL not running and RSB=100Hz. A corrective factor $\pi/\sin(\pi \cdot 0.165)$ has been applied to take into account the square wave modulation. The horizontal line is the average value of the data points.

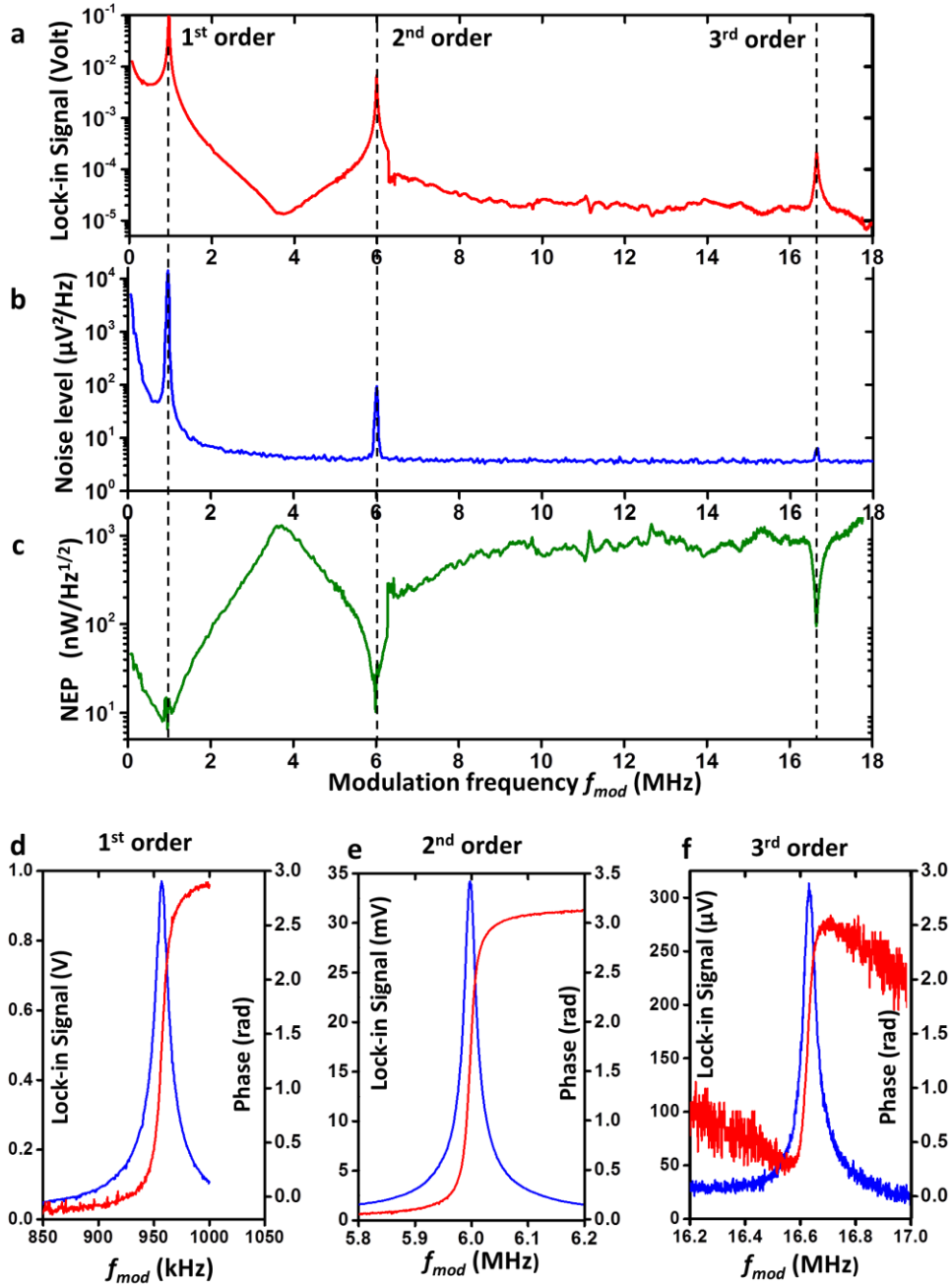


Figure 4: Performance as a function of the modulation frequency **a**, Lock-in signal R recorded with in a wide sweep of the modulation frequency f_{mod} of the QCL drive current (see Fig. 3a) and maximum output THz power of 4.7mW. **b**, Brownian motion of the cantilever, recorded with the ESA and without the , in the same frequency range as above. **c**, NEP as a function of f_{mod} obtained by the ratio between the square root of the noise $S_{xx}(f_{mod})$ from the data in 4b and the signal R from the data 4a. The small features around the mechanical resonances at 0.95MHz, 6MHz and 16.6MHz arise from a slight mismatch between the measurements of f_{mod} with the ESA and the lock-in amplifier. **d,e,f**, High resolution scans of the lock-in signal (R) and phase (ϕ), when the modulation frequency f_{mod} is varied around the cantilever mechanical resonances.

Methods

Sample fabrication protocol.

The composition of the wafers used to fabricate our structures is the following: a semi-insulating GaAs substrate, epitaxially grown GaAs 320 nm buffer layer, a 1.6 μm Al_{0.8}Ga_{0.2}As sacrificial layer, and a 320 nm GaAs top layer. The structures are defined by e-beam lithography on PMMA 950 resist. After revealing the resist, a layer of 5 nm of platinum (Pt) and 150nm of gold (Au) are evaporated on the sample. Then, a lift-off is performed in order to define the metallic patterns that will serve as an etch mask for dry etching in an inductively coupled plasma reactor. In this step the top GaAs and AlGaAs sacrificial layer are removed everywhere but under the features protected by the metal. The sample is then wet etched in a refrigerated (4°C) dilute HF 2.5% solution for 45s, which allows removing anisotropically the sacrificial layer of AlGaAs with a depth to lateral etching ratio of 1.3. To avoid the sticking of the cantilever to the substrate, the sample is put on a hot plate at 200°C for 60 s.

THz spectroscopy of SRR.

To infer the THz resonances of our split ring resonators, we have been characterized in transmission measurements with a Fourier Transform Interferometer (FTIR). The schematics of this experiment is shown in the Supplementary figures Fig.1a. In this experiment, the radiation of the Globar source of the FTIR was focused and collected from the structure with four F1 parabolic mirrors, and detected by a cooled Ge bolometer. A polarizer placed on the exit of the FTIR allows to select the polarization of the incident beam. The whole set-up is placed in dry air environment in order to minimize water absorption in the THz spectra. The transmission measurements were performed on a dense array of resonators, as shown in Supplementary figures Fig. 1b with 5 μm spacing between the structures, in order to obtain clear signatures of the resonances in the transmission spectra [3,22]. Indeed, the typical beam spot in the system was on the order of 1mm², which was much larger than the typical cross section of a single resonator (4x10⁻⁴mm²). The spectra have been normalized on a reference obtained on the semiconductor substrate without any structures, and a baseline correction has been applied.

In Fig. 2a, the SRR resonance appears as a transmission dip at 2.68 THz. This resonance of the structure can be well recovered by the formula: $\omega_{\text{THz}} = \pi c / n_{\text{eff}} P$, with c is the speed of light, $P = 44.5 \mu\text{m}$ the medium perimeter of the resonator in Fig. 1 and n_{eff} is an effective index. This formula assumes a $\lambda/2$ standing wave pattern with electric field antinodes at the plate sides of the SRR (Fig. 1a, inset). Knowing the frequency $\omega_{\text{THz}}/2\pi = 2.68$ we obtain an effective index $n_{\text{eff}} = 1.27$. This value compares well to the refractive index $(1.0 + (1 - \alpha) \cdot n_{\text{AlGaAs}}) / 2 = 1.21$, where α is the ratio between the length of the cantilever (suspended part) and the perimeter P . This latter averages between the air and the refractive index of the AlGaAs layer below the resonator with an index $n_{\text{AlGaAs}} = 3.18$.

Detection of the cantilever motion.

The cantilever motion is measured in an optical detection scheme with a near infrared (NIR) $\lambda=940\text{nm}$ laser diode. The laser beam is focused on the cantilever through a microscope objective. The fraction of the NIR beam reflected by the cantilever was sent through a sharp edge blade and measured by a balanced photo-detection unit connected to a spectrum analyzer (SA). The SA provides the spectral components of the noise power density of the cantilever displacement $S_{xx}(f)$ [8]. In the set-up where the SRR was coupled with a modulated THz QCL (Fig. 3), the output of the balanced detection was either sent to a spectrum analyzer, or to a lock-in amplifier referenced to the QCL modulation frequency f_{mod} .

Mechanical characteristics of the cantilever.

The geometry and material composition of our cantilever resonator is indicated in the Supplementary figures Figure 2. The length $L=17.2\mu\text{m}$ of the cantilever is measured from the free end to the mid-point of the etched pedestal. Regarding the cantilever as a homogeneous beam, the resonant of the first in-plane flexural mode is described by the equation [24] $f_1=0.162(w/L^2)(Y/\rho)^{1/2}$. Here Y is the Young's modulus and ρ the volume density of the cantilever. Neglecting the 5nm Pt adhesive layer indicated in Supplementary figures Fig. 2, the main constituents of the cantilever are Gold (Au) and GaAs, with the following characteristics:

$$\text{Au} \begin{cases} Y_{\text{Au}} = 79\text{GPa} \\ \rho_{\text{Au}} = 19.3\text{g/cm}^3 \end{cases}, \quad \text{GaAs} \begin{cases} Y_{\text{GaAs}} = 85.5\text{GPa} \\ \rho_{\text{GaAs}} = 5.3\text{g/cm}^3 \end{cases}$$

As the Gold and GaAs have very similar Young's modulae, we take the average $Y=0.5(Y_{\text{Au}}+Y_{\text{GaAs}})=82.25\text{GPa}$. Similarly, we use a mean density averaged over the thickness of the different materials: $\rho = (\rho_{\text{Au}}t_1 + \rho_{\text{GaAs}}t_2)/(t_1+t_2) = 9.8\text{g/cm}^3$. Using these values, we obtain a numerical estimate $f_1=922\text{kHz}$, which compares very well with the experimental value 957 kHz, considering the fact that dimension are known with 10% uncertainty. This accordance justifies our approach of using average density for the cantilever. With respect to the model from paragraph 1 it is also useful to define an effective mass m_{eff} of the cantilever according to the formula [8] $m_{\text{eff}} = (33/140)\rho wt = 10.8\text{pg}$. The frequency can thus be re-expressed as $f_1 = (1/2\pi)(k/m_{\text{eff}})^{1/2}$ where $k = Ytw^3/6L^3 = 0.25\text{N/m}$. Using the parameters k and m_{eff} defined above, we can treat the cantilever as one dimensional harmonic oscillator. Within this picture, we can also express the noise spectral density of the Brownian motion of the cantilever $S_{xx}(f)$ as a function of the frequency [8]:

$$S_{xx}(f) = \frac{2k_B T \Gamma_m}{m_{\text{eff}} (2\pi)^3} \frac{1}{(f^2 - f_1^2)^2 + (f \Gamma_m)^2}$$

Fitting the experimental data of the Brownian motion with the above equation allows to determine precisely the parameters f_1 and Γ_m , and hence the quality factor $Q_m = f_1 / \Gamma_m$. As the effective mass $m_{\text{eff}} = 10.8 \text{ pg}$ reproduces well the resonant frequency, we can use it to determine the peak value of the noise spectral density:

$$S_{xx}(f = f_1) = \frac{2k_B T Q_m}{m_{\text{eff}} (2\pi)^3 f_1^3} = 0.33 \text{ pm}^2 / \text{Hz}$$

This value is used to calibrate the readings from the spectral analyzer, as described in the main text.

THz optomechanical coupling and effective capacitance

The coupling between the SRR and the cantilever movement can be described in the picture of an equivalent LC circuit [12,14]. The electric field of the structure is described by an equivalent capacitor $C(x)$ which is a function of the cantilever displacement x . The dynamical variables of the coupled system are x , the displacement of the cantilever tip, and q , the charge induced on the capacitor plates. Then the Lagrangien \mathcal{L} of the system is written as:

$$\mathcal{L} = \frac{1}{2} m_{\text{eff}} \dot{x}^2 + \frac{1}{2} L \dot{q}^2 - \frac{q^2}{2C(x)} - \frac{1}{2} m_{\text{eff}} \omega_m^2 x^2. \text{ The cantilever movement can then be}$$

provided, for instance, by the Lagrange equation for the position:

$$m_{\text{eff}} \frac{d^2 x}{dt^2} + \frac{m_{\text{eff}} \omega_m}{Q_m} \frac{dx}{dt} + m_{\text{eff}} \omega_m^2 x = \frac{d}{dx} \left(\frac{q^2}{2C(x)} \right)$$

Usually, the displacement of the cantilever x is small compared to the gap d_{gap} , therefore the derivative in the r.h.s. can be approximated at zeroth order with its value at $x=d_{\text{gap}}$. Using the expression of the electrical energy density of the resonator $W_{\text{THz}} = q^2/2C(x)$, and introducing an effective gap through the formula $d_{\text{gap}}^{\text{eff}} = ((d \ln C(x) / dx)|_{x=d_{\text{gap}}})^{-1}$ we arrive at the results stated in the main text. The parameter $d_{\text{gap}}^{\text{eff}}$, defined above, allows to evaluate the magnitude of the Coulomb force for an arbitrary geometry. However, its exact evaluation is difficult in practice, due to the fringing fields of the capacitance. We have used an analytical expression provided in Ref.25:

$$C(x) \propto \frac{t}{x} + \frac{1}{\pi} \left[1 + \ln \left(\frac{2\pi t}{x} \right) + \ln \left(1 + \frac{2w}{x} + 2\sqrt{\frac{w}{x} + \frac{w^2}{x^2}} \right) \right]$$

This first term is the capacitance per unit length of a planar plate capacitor with plate width b and a thickness x , while the following terms are correction due to the finite width b and thickness w of the plates. Constant factors have been discarded due to the logarithm in the definition of $d_{\text{gap}}^{\text{eff}}$. Numerical derivation with the parameters $w=581 \text{ nm}$ and $t=470 \text{ nm}$ provide

$d_{\text{gap}}^{\text{eff}} = 546 \text{ nm}$ for $x = d_{\text{gap}} = 309 \text{ nm}$. The fact that the effective gap is greater than the physical gap is understandable, since the fringing fields which “run away” from the structure are expected to be less sensitive to the cantilever displacement with respect to the field confined in the gap. Note also that in the actual resonance the charge density develops along the whole cantilever length owe to propagation effects. We have considered only the charges in the vicinity of the gap, since the effects of the other parts are expected to be small as the distance between the positive and negative charges is much larger than d_{gap} .

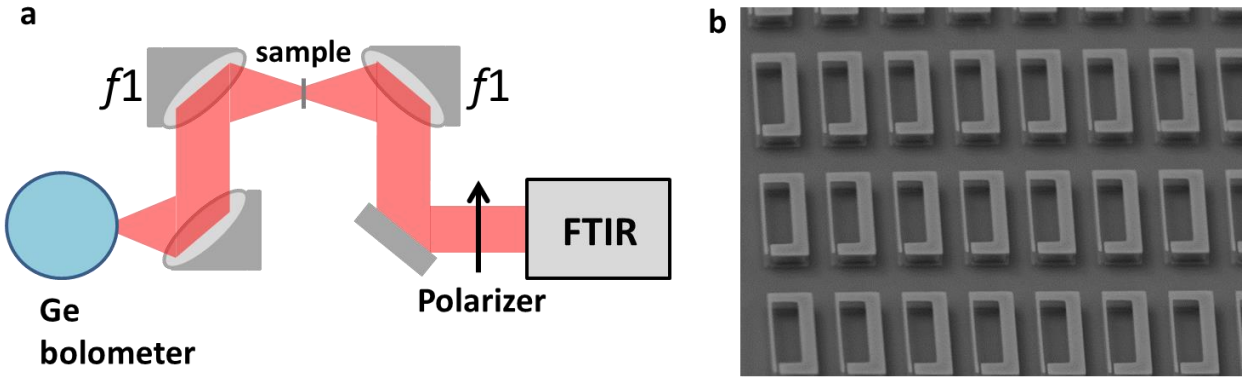
THz QC Laser characteristics and intensity modulation

The QCL used in this experiment has an active region similar to the one described in Refs. **27** and **28**. It was processed in a single metal ridge waveguide of 3mm length, with a current threshold $I_{\text{th}} = 1.0 \text{ A}$ delivering powers on the order of mW when stabilized in temperature around 20K. The optical power delivered by the laser was measured with a calibrated THz power meter (Ophir 3A-P-THz ROHS). In Supplementary figures Fig. 3 we show the spectrum of the QCL, recorded at $V = 48.5 \text{ V}$ superimposed with the transmission spectrum of the SRR array from Supplementary figures Fig. 2b. The QCL had a central emission frequency of 2.6 THz, slightly detuned from the SRR resonance.

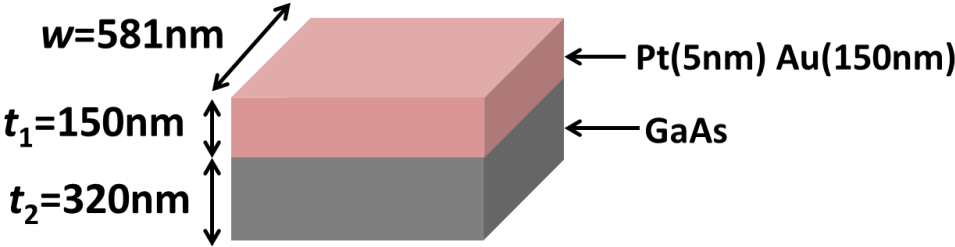
To achieve an intensity modulation for the driving THz force on the cantilever, the driving current of the QCL was modulated in a square wave with a duty cycle of 16.5% from the threshold I_{th} to a maximal value. In Supplementary figures Fig. 4 we show the time trace of the driving current (red curve) obtained with an electronic oscilloscope. When the modulation frequency was matched with the mechanical frequency of the cantilever, the latter responded with a sine-wave (blue curve). This signal was represent the time trace of the PhDs detector voltage, which is proportional to the cantilever displacement. This means that the mechanical resonator responds to the first Fourier harmonic of the intensity square wave intensity modulation. The first harmonic has an amplitude that is $\sin(0.16\pi)/\pi$ of the square wave amplitude, which justifies the correction factor provided in the legend of Fig. 3 of the main text.

To verify the resonant interaction between the source and the THz source, we also performed a detection experiment described in the main text with another QCL, which was emitting at 2 THz and therefore detuned from the SRR resonance. The 2THz QCL delivered a maximum power of 1mW and was operated in the same conditions as the 2.7 THz QCL: pulsed mode with a 16.5% duty cycle and 957KHz modulation frequency. As expected, we did not observe any coherent signal from this laser, as it was set away from the SRR resonance and it did not excite the charge oscillation that lead to a mechanical force on the cantilever.

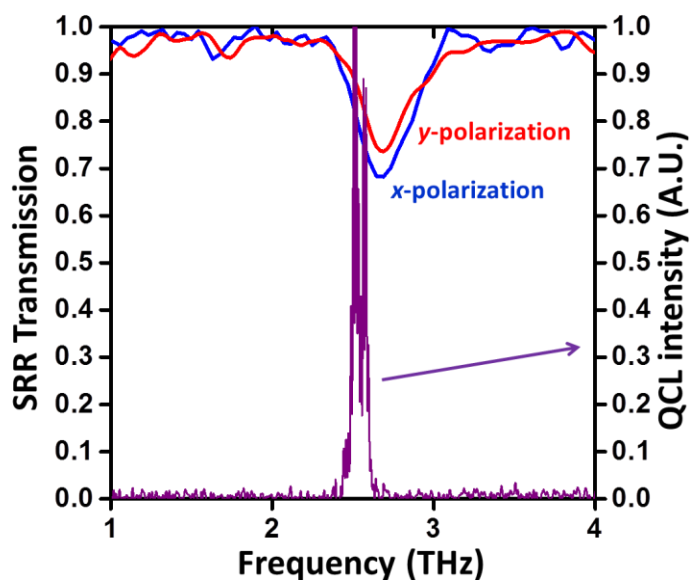
Supplementary figures



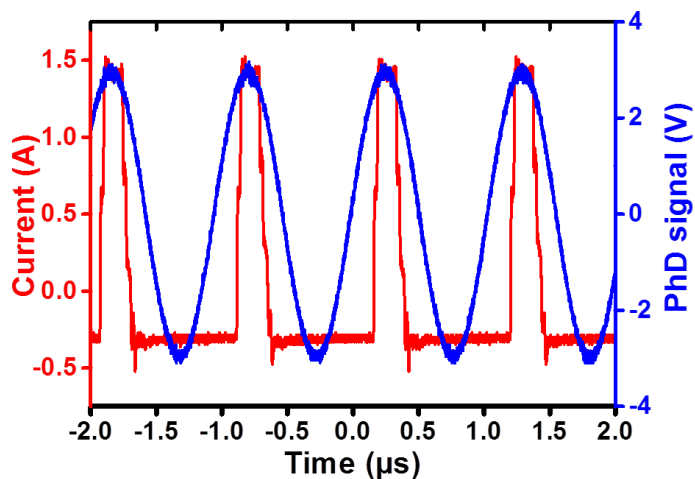
Supplementary Figure 1: THz transmission spectroscopy **a**, Experimental setup used for the transmission measurements on the SRR samples. **b**, Scanning electron microscope image of a dense array of identical resonators used for the transmission experiments.



Supplementary Figure 2: Schematics of the cross section of the cantilever part



Supplementary Figures 3: QCL and SRR spectra. QCL emission spectrum superposed with the transmission spectrum of the SRR arrays from Supplementary Fig. 1b. “x/y-polarization” refer to transmission measurements with an electric field vector along the x/y axis as defined in Fig.2. In our experiments, the laser electric field was along the x-direction.



Supplementary Figure 4: Time traces representative of the incident THz intensity and the corresponding mechanical response of the cantilever. In red: QCL driving current. In blue: signal from the balanced photo detection unit, recorded on an electronic oscilloscope.